RESEARCH ARTICLE
SOLID EARTH: GEOELECTROMAGNETICS

Earth and Planetary Physics
9: 1–13, 2025
doi: 10.26464/epp2025030

MSCM: A geomagnetic model derived from Swarm, CSES, and MSS-1 satellite data and the evolution of the South Atlantic Anomaly

Yu Gao[1,2], ZhengTao Wang[1,3*], Philip W. Livermore[2], Hannah F. Rogers[2], and Cong Liu[1]

[1]School of Geodesy and Geomatics, Wuhan University, Wuhan 430079, China;

[2]School of Earth and Environment, University of Leeds, Leeds LS2 9JT, United Kingdom;

[3]Hubei Luojia Laboratory, Wuhan 430079, China

Key Points:

- We present a geomagnetic field model, MSCM, that integrates vector and scalar data from the Swarm, China Seismo-Electromagnetic Satellite (CSES), and Macau Science Satellite-1 (MSS-1) missions.
- The MSCM is a novel application of both CSES vector data and MSS-1 data in a smoothed, fully time-dependent model.
- Using the MSCM, we show newly identified west–east differences in the behavior of the South Atlantic Anomaly.

Citation: Gao, Y., Wang, Z. T., Livermore, P. W., Rogers, H. F., and Liu, C. (2025). MSCM: A geomagnetic model derived from Swarm, CSES, and MSS-1 satellite data and the evolution of the South Atlantic Anomaly. *Earth Planet. Phys.*, *9*(3), 1–13. http://doi.org/10.26464/epp2025030

Abstract: Measurements from geomagnetic satellites continue to underpin advances in geomagnetic field models that describe Earth's internally generated magnetic field. Here, we present a new field model, MSCM, that integrates vector and scalar data from the Swarm, China Seismo-Electromagnetic Satellite (CSES), and Macau Science Satellite-1 (MSS-1) missions. The model spans from 2014.0 to 2024.5, incorporating the core, lithospheric, and magnetospheric fields, and it shows characteristics similar to other published models based on different data. For the first time, we demonstrate that it is possible to successfully construct a geomagnetic field model that incorporates CSES vector data, albeit one in which the radial and azimuthal CSES vector components are Huber downweighted. We further show that data from the MSS-1 can be integrated within an explicitly smoothed, fully time-dependent model description. Using the MSCM, we identify new behavior of the South Atlantic Anomaly, the broad region of low magnetic field intensity over the southern Atlantic. This prominent feature appears split into a western part and an eastern part, each with its own intensity minimum. Since 2015, the principal western minimum has undergone only modest intensity decreases of 290 nT and westward motion of 20 km per year, whereas the recently formed eastern minimum has shown a 2–3 times greater intensity drop of 730 nT with no apparent east–west motion.

Keywords: geomagnetism; Swarm; CSES; MSS-1; geomagnetic field model

1. Introduction

Earth's magnetic field is a complex system involving multiple sources: from the core, lithosphere, ionosphere, and magnetosphere, over a range of spatial and temporal scales (Constable and Constable, 2023). The strongest source is Earth's core, where the magnetic field is generated by the geodynamo process, driven by the convection of electrically conductive liquid iron in the outer core (Hulot et al., 2010). Its temporal variations, known as the geomagnetic secular variation (SV), reflect the slow evolution of the geomagnetic field and provide critical insights into the geodynamo mechanism. Studying these changes requires separating the core field from other magnetic sources and monitoring it over extended periods. Satellites are essential for observing Earth's magnetic field globally, providing time-series data long enough to analyze decadal variations in the core field with continuous coverage since 1999. Global geomagnetic field models, built using satellite data, have provided new and unprecedented insights into the geodynamo (Finlay et al., 2023).

First author: Y. Gao, ygaosgg@whu.edu.cn
Correspondence to: Z. T. Wang, ztwang@whu.edu.cn
Received 16 JAN 2025; Accepted 25 FEB 2025.
First Published online 31 MAR 2025.

Current monitoring of the geomagnetic field by advanced satellite technology has built on the successes of previous geomagnetic missions over the last few decades, including Ørsted (Neubert et al., 2001) and Challenging Minisatellite Payload (CHAMP; Rygaard-Hjalsted et al., 2000). At present, three missions are collecting both scalar and vector geomagnetic data: the Swarm (Olsen et al., 2013), China Seismo-Electromagnetic Satellite (CSES; Yang YY et al., 2021b), and Macau Science Satellite-1 (MSS-1; Zhang K, 2023; Livermore et al., 2024) missions. Their high-precision observations enable detailed investigations into Earth's magnetic field and its underlying processes (Whaler et al., 2022; Finlay et al., 2023).

The Swarm mission, launched on November 22, 2013, consists of three low-Earth orbit satellites — Swarm Alpha, Bravo, and Charlie

(A, B, and C) — designed to provide comprehensive magnetic field observations (Olsen et al., 2013). Swarm A and C form a lower pair of satellites, flying side-by-side with a 1.4° separation in longitude at the equator, at an initial altitude of 462 km and an inclination of 87.35°, whereas Swarm B orbits independently at a higher altitude of 511 km, with an inclination of 87.75°. The Swarm satellites are equipped with the Absolute Scalar Magnetometer (ASM) and the Vector Field Magnetometer to conduct high-precision, high-resolution measurements of the magnetic field. The primary goal of the Swarm mission is to provide the best survey of the global geomagnetic field and its temporal variations, offering valuable insights into the Earth's interior and its surrounding environment.

The CSES, launched on February 2, 2018, is positioned in a near-polar, Sun-synchronous orbit with an initial altitude of 507 km and an inclination of 97.4° (Shen XH et al., 2018). It features a 5-day revisiting period. The satellite is equipped with a high-precision magnetometer package, which includes a dual Fluxgate Magnetometer (FGM) for measuring the vector field and a Coupled Dark State Magnetometer (CDSM) for measuring the scalar field. The objective of the CSES is to collect data on electric and magnetic fields, as well as plasma and high-energy particles, to support the study of signals related to earthquakes, geophysics, and space science. Compared with the Swarm satellite data, the quality of the magnetic field data from the CSES is lower, particularly in the high southern latitudes. The quality gradually improves toward the equator and is relatively better in the northern latitudes (Yang YY et al., 2021a).

The MSS-1 mission, launched on May 21, 2023, consists of two satellites, the MSS-1A and MSS-1B, placed in near-circular orbits with a 41° inclination at an altitude of 430 km. The MSS-1A maintains a stable circular orbit to ensure consistent measurements, whereas the MSS-1B has transitioned to a slightly elliptical orbit, ranging from 400 to 500 km, to improve ionospheric sampling at different altitudes (Zhang K, 2023). The MSS-1A is equipped with vector and scalar magnetometers as its primary instruments, whereas the MSS-1B, a smaller cube-shaped satellite approximately 3 m in size, carries instruments designed to measure plasma density and energetic electrons (Livermore et al., 2024). One of the main aims of the mission is to measure and map the evolution of the South Atlantic Anomaly (SAA), a region of low magnetic intensity stretching broadly between Africa and South America. Over the past 200 years, the SAA has been expanding and drifting southwest (Amit et al., 2021), with its minimum intensity decreasing at a rate of approximately 30 nT per year (Kakad and Kakad, 2022). The SAA is important for the environment of near-Earth space because it is linked to locally enhanced radiation and equipment malfunction on spacecraft (Domingos et al., 2017; Heirtzler, 2002). The equatorial focus of the MSS-1 orbit is ideal for studying the temporal evolution of this feature. Figure 1 illustrates a comparison of the orbital distribution of the Swarm A satellite, CSES, and MSS-1A over one day.

Despite the advances in satellite measurement, the observational datasets remain sparse, and using them to constrain geomagnetic field models provides a tool not only to interpolate between the data, but also downward to continue the data through the mantle to study the time dependence of core field variations. In the last decade, a variety of field models have been produced using a range of methodologies and datasets. The CHAOS series of models represents Earth's time-dependent geomagnetic field from 1999 (Olsen et al., 2014; Finlay et al., 2020), constrained by both ground-based observatory and satellite data. The CHAOS-7 model (Finlay et al., 2020) represents the core field from 1999 to 2024 using satellite data from Ørsted, CHAMP, SAC-C (Satélite de Aplicaciones Científicas-C), CryoSat-2, and Swarm; it is parameterized by spherical harmonics smoothed by minimizing the second- and third-order temporal derivatives. The CHAOS-8 model, the latest generation, extends the CHAOS-7 model by incorporating CSES scalar data and MSS-1 vector data (Kloss et al., 2024), but it uses dynamo *a priori* information rather than explicit smoothing to regularize the spherical harmonic coefficients. The comprehensive models (CMs), based on Ørsted, CHAMP, SAC-C, and Swarm, offer a continuous core field representation from 1999 to 2019.5, inverting simultaneously for sources from the core, lithosphere,

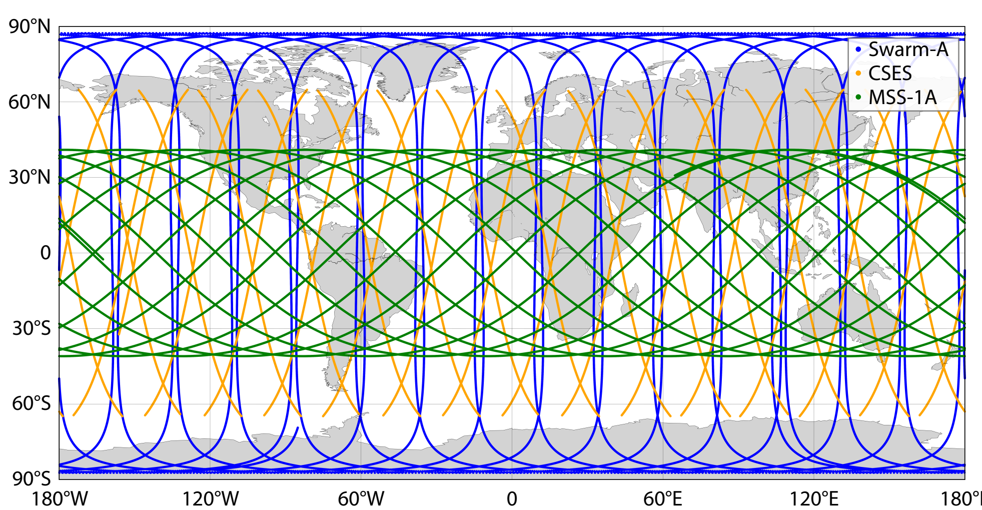

Figure 1. Comparison of orbit trajectories over one day for the Swarm A, CSES, and MSS-1A spacecraft. Although CSES is on a polar orbit, only data between −65° and 65° are currently available.

oceanic tidal components (M_2, N_2, and O_1), ionosphere, magnetosphere, and associated induced magnetic fields (Sabaka et al., 2015, 2020). The Kalmag model, utilizing Kalman filtering and smoothing algorithms, provides a methodologically different (second-order autoregressive) approach, spanning from 2000.5 to 2022.2 (Baerenzung et al., 2022). The CSES global geomagnetic field model (CGGM) utilizes magnetic field data from the CSES alone to describe the Earth's main magnetic field and its linear temporal evolution over the period from March 2018 to September 2019 (Yang YY et al., 2021a). Finally, the Macau Scientific Satellite-1 Initial Magnetic Field Model (MIFM) characterizes both lithospheric anomalies and the linearly time-dependent core surface field by using data from the MSS-1 and Swarm (Jiang Y et al., 2024).

Despite the differences in data sources, data selection, and model construction highlighted by the aforementioned range of models, geomagnetic field models largely agree on the large-scale behavior of the SV and core field (Alken et al., 2021), indicating its robustness under the different modeling choices. However, differences in the models do persist, particularly at small length-scales and rapid timescales, indicating the importance of making the most effective use of the data available.

In this work, we introduce a new geomagnetic model over the span from 2014.0 to 2024.5 called MSCM: a model defined by using vector and scalar data from the Swarm, CSES, and MSS-1 missions. Our aims are threefold. First, we aim to test whether it is possible to use CSES vector data with other data sources to build a global model. In a previous study, Yang YY et al. (2021a) constructed a model based purely on CSES data, but it is unclear whether it can be integrated successfully into a broader dataset. Second, we aim to test whether we can include MSS-1 data into a fully time-dependent smoothed geomagnetic field model by building on successful studies in which MSS-1 data have been incorporated into a temporally linear initial field model (Jiang Y et al., 2024) or the CHAOS-8 model regularized by using dynamo priors (Kloss et al., 2024). Last, we aim to use our new model to study the evolution of the SAA over the last decade.

The article is structured as follows. In Section 2, we outline the criteria for data selection and describe the modeling strategy utilized in the MSCM model. In Section 3, we introduce the magnetic sources considered, the parameterization of the MSCM model, and our algorithm for model fitting. We present our new model in Section 4, including data misfit statistics, model diagnostics, and comparisons with other models. We end with a discussion of new geophysical insights into the SAA and present our conclusions on how best to use both the MSS-1 and CSES data.

2. Data

In our study, we use data from three independent satellite missions: Swarm, CSES, and MSS-1. Although we report our model over the period from 2014.0 to 2024.5, our model is fit to data over the slightly longer period of November 25, 2013, to September 30, 2024. Below, we summarize the data used from the three missions and describe our data selection procedure.

2.1 Swarm Data

From the Swarm satellite mission, we use vector and scalar data (versions 0602/0605/0606) from three satellites: Swarm A and Swarm B for the period between November 25, 2013, and September 30, 2024, and Swarm C for the period between November 25, 2013, and November 5, 2014. No data were used from Swarm C after November 5, 2014, because of an ASM instrument malfunction. We noted that during July and August 2023, both Swarm A and Swarm B had several orbital changes, including multiple collision avoidance and return maneuvers, and they occasionally operated the ASM in burst mode (Stevanović et al. 2023). These issues meant not only that the number of usable data points was small (see Figure 2), but also that the data contained substantial unmodeled signals (as we show in Section 2.4). For Swarm A, Swarm B, and Swarm C, we use calibrated scalar and vector data, which were subsampled to 1-minute intervals.

2.2 CSES Data

From the CSES mission, with data availability limited to latitudes below ±65°, we utilize vector and scalar data between January 2019 and April 2021. However, no scalar data were available

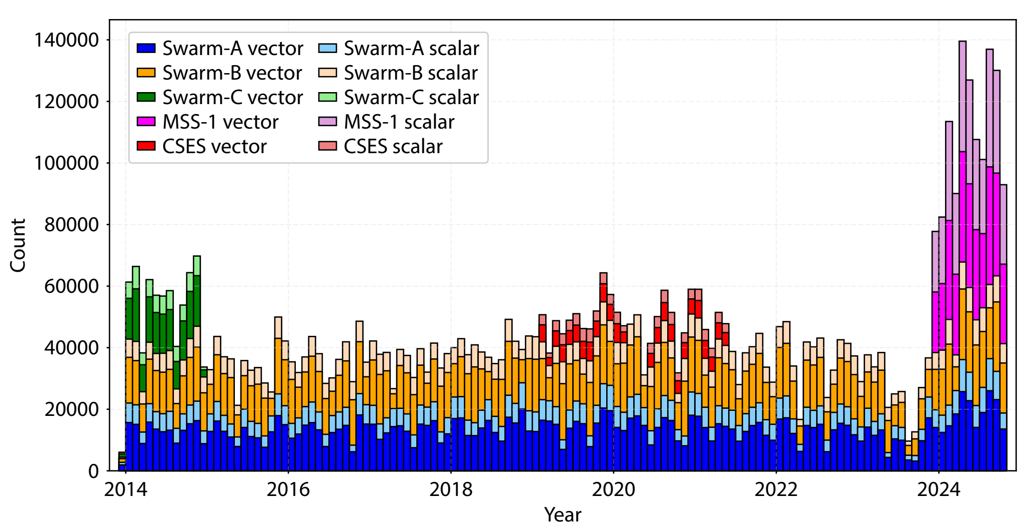

Figure 2. Monthly count of scalar and vector data, after data selection, for each satellite mission.

between February and April 2020, resulting in data gaps during these months (see the dashed red line in Figure 4). These data, initially sampled at 1-second intervals, were subsampled to 1-minute intervals. The calibrated scalar and vector data include temperature and linear corrections from ground calibration. The calibration also applies a steering error correction for total field detection, along with an orthogonal correction, the removal of magnetic interference, and coordinate transformations (Yang YY et al., 2024).

2.3 MSS-1 Data

From the MSS-1 mission, with coverage restricted to latitudes below ±40°, we use vector and scalar data from the MSS-1A satellite for the period between November 2, 2023, and August 31, 2024. These data were also subsampled to 1-minute intervals. The scalar and vector data are calibrated by using Euler angle estimation to correct the misalignment between the satellite's magnetometer and star tracker reference frames (Yan Q et al., 2023).

2.4 Data Selection

To minimize the influence of field-aligned currents in polar regions during modeling, satellite data were divided into nonpolar and polar subsets based on quasi-dipole (QD) latitude (Richmond, 1995); we defined nonpolar data by QD latitude ≤55° for Swarm and MSS-1, whereas challenges with CSES data highlighted by Yang YY et al. (2021a) limited us to ≤20°. Polar data were defined by all other (higher) latitudes. Vector and scalar data were used at low latitudes, whereas only scalar data were used at high latitudes. Data from each subset were selected under quiet geomagnetic conditions according to specific criteria common to each satellite mission.

Nonpolar subset data selection was based on the following criteria:
- *Kp* index ≤2°;
- Only data from dark regions (sun at least 10° below the horizon);
- RC index rate of change in absolute terms ≤2 nT/h (Olsen et al., 2014).

Polar subset data selection was based on the following criteria:
- Only data from dark regions (sun at least 10° below the horizon);
- RC index rate of change in absolute terms ≤2 nT/h;
- Merging of the electric field at the magnetopause E_m ≤2.4 mV/m, averaged over the previous 2 hours;
- Interplanetary magnetic field (IMF) component $B_{\mathrm{IMF},z}$ in GSM coordinates positive on average over the previous 2 hours.

For CSES data, we imposed a quality control measure of removing any data for which the magnitude of the vector difference compared with a prediction from the CHAOS-8 model exceeded 100 nT. Additionally, any data flagged with *FLAG_TBB* = 1 were excluded. This flag indicates magnetic disturbances caused by the Tri-Band Beacon (TBB) instrument, which produces an unmodeled signal measured by the FGM, which manifests as biased noise that we cannot remove (Yang YY et al., 2021b).

After data selection, our MSCM model was defined by using 3 × 1,367,511 vector data points and 1,726,813 scalar data points. When model fitting, all satellite data were also weighted proportionally to sinθ, where θ is geographic colatitude, simulating an equal-area distribution. Figure 2 shows the number of data points contributing to the MSCM model as a function of time, separated according to either scalar or vector data from each mission.

3. Model Parameterization and Estimation

Separating the various magnetic sources whose sum defines the measured geomagnetic signal is challenging because of their overlapping spatial and temporal scales. Numerically, separation of these contributions requires appropriate temporal parameterization for each source. The MSCM modeling approach builds on the CHAOS-7 model (Finlay et al., 2020), in which we describe the core field, lithospheric field, and magnetospheric field, including its induced field. We do not take into account the ionospheric field or any other fields induced in the oceans and solid earth.

3.1 Internal Field

The Earth's internal magnetic field includes the core and lithospheric fields and can be expressed as a spherical harmonic expansion:

$$V^{\mathrm{int}}(r,\theta,\phi,t)=a\sum_{n=1}^{N^{\mathrm{int}}}\sum_{m=0}^{n}\left(\frac{a}{r}\right)^{n+1}\left[g_n^m(t)\cos m\phi+h_n^m(t)\sin m\phi\right]P_m^m(\cos\theta), \tag{1}$$

where a is the Earth radius, equal to 6371.2 km, and (r,θ,ϕ) represent the radial distance, colatitude, and longitude, respectively, in the spherical geographical coordinate system. The term $P_n^m(\cos\theta)$ defines the Schmidt seminormalized associated Legendre functions of degree n and order m (Winch et al., 2005), whereas $\{g_n^m(t),h_n^m(t)\}$are the Gaussian coefficients describing internal sources truncated at $N_{\mathrm{int}}=40$. We represent the time-dependent core field by using degrees 1–15, whereas degrees 16–40 represent the time-independent lithospheric field.

The time-dependent coefficients $\{g_n^m(t),h_n^m(t)\}$ are parameterized in terms of B-splines (De Boor, 1978). For example,

$$g_n^m(t)=\sum_{i=1}^{I}g_{n,i}^mB_{k,i}(t), \tag{2}$$

where $B_{k,i}(t)$ for$i=1,2,\cdots,I$ are predefined order-6 B-splines and $g_{m,i}^m$ are the B-spline coefficients. The B-spline basis functions are defined on knots at 6-month intervals and six-fold multiplicity at the model endpoints at $t_s=2013.8$ and $t_e=2024.8$.

3.2 External Potential Fields

To describe the external (magnetospheric) and corresponding Earth-induced fields, we adopt the parameterization of the CHAOS-7 model (Finlay et al., 2020) based on spherical harmonics. The scalar potentials for near- and far-magnetospheric sources were truncated at degrees $N_{\mathrm{near}}=2$ and $N_{\mathrm{far}}=2$, respectively. We coestimate, along with the internal field, the static regression factors $\hat{q}_1^0,\hat{q}_1^1,\hat{s}_1^1$ and the time-varying RC baseline corrections $\Delta q_1^0,\Delta q_1^1$ and Δs_1^1 in bins of 30 days.

3.3 Model Estimation

Our least squares estimation approach minimizes a cost function, a combination of data residuals and regularization terms:

$$[\boldsymbol{g}(\boldsymbol{m}) - \boldsymbol{d}]^{\mathrm{T}} C_d^{-1} [\boldsymbol{g}(\boldsymbol{m}) - \boldsymbol{d}] + \lambda_3 \boldsymbol{m}^{\mathrm{T}} \underset{=3}{\Lambda} \boldsymbol{m} + \lambda_2 \boldsymbol{m}^{\mathrm{T}} \underset{=2}{\Lambda} \boldsymbol{m}, \tag{3}$$

where $\boldsymbol{g}(\boldsymbol{m})$ represents model predictions based on geomagnetic field model coefficients $\boldsymbol{m}$, $\boldsymbol{d}$ are the observed data, and C_d^{-1} is the inverse of the data error covariance matrix (Holme and Bloxham, 1996). The matrices $\underset{=3}{\Lambda}$ and $\underset{=2}{\Lambda}$ are the inverses of the *a priori* model covariance matrices (also sometimes called the regularization matrices), which penalize the squared values of the third and second time derivatives of the radial field B_r at the core surface, respectively. Specifically, $\boldsymbol{m}^{\mathrm{T}} \underset{=3}{\Lambda} \boldsymbol{m}$ implements the squared third time derivative of the internal radial field across the core surface and integrated over the time span of the model, and $\boldsymbol{m}^{\mathrm{T}} \underset{=2}{\Lambda} \boldsymbol{m}$ implements the squared second time derivative only at the model endpoints t = 2013.8 and 2024.8.

Although the vector data are linearly related to the model $\boldsymbol{m}$, the scalar intensity data are nonlinearly related to the Gaussian coefficients. Overall, Equation (3) is nonlinear and not quadratic, and it cannot be directly minimized in a single step. Instead, we use an iterative Gauss–Newton approach, at each step solving the linearized system. The data error covariance matrix is estimated by using an iteratively reweighted least squares algorithm incorporating Huber weights (Constable, 1988; Sabaka et al., 2020) to enhance the robustness against outliers. In the ith iteration, outliers were downweighted by assigning lower weights to residuals exceeding the threshold $c\sigma_i$. The weights $w_{i,k}$ for the kth residual were calculated as

$$w_{i,k} = \frac{1}{\sigma_i^2} \min\left(\frac{c\sigma_i}{|e_{i,k}|}, 1\right) \tag{4}$$

(Sabaka et al., 2020), where $e_{i,k}$ is the residual of the kth observation in the ith iteration, and σ_i is the standard deviation of the residuals in the ith iteration. We chose the threshold parameter (c) to equal 1.5.

The regularization parameters λ_3 and λ_2 then determine the strength of temporal regularization. The choice of λ_2 and λ_3 is subjective and defines the smoothness of the model. We tested several values for the parameters and chose λ_2 = 50 (nT/year^2)$^{-2}$. Additionally, we applied a special treatment to the time-dependent coefficients, allowing $\lambda_3 = \lambda_3^{\mathrm{lat}}(n) \times \lambda_3^{\mathrm{long}}(m)$ to vary with spherical harmonic degree and order (n, m):

$$\lambda_3^{\mathrm{lat}}(n) = \begin{cases} 1, & n < n_{\min} \\ \dfrac{0.995}{2}\left[1 + \cos\left(\pi \dfrac{n - n_{\min}}{n_{\max} - n_{\min}}\right)\right] + 0.005, & n_{\min} \leqslant n \leqslant n_{\max} \\ 0.005, & n > n_{\max} \end{cases}, \tag{5}$$

where $n_{\min}$ = 3 and $n_{\max}$ = 6 are the chosen limits of a half-cosine taper (Kloss, 2021). In addition to the degree-dependent temporal regularization, zonal and nonzonal coefficients were treated differently as

$$\lambda_3^{\mathrm{long}}(m) = \begin{cases} 0.3, & m = 0 \\ 0.03, & m \neq 0 \end{cases}. \tag{6}$$

These parameter choices are ultimately subjective but were based on the methodology of CHAOS-7 (Finlay et al., 2020). They were chosen such that our model was approximately consistent with the CHAOS-7 and CHAOS-8 models, in terms of spatial power spectra and time-dependent features.

4. MSCM Diagnostics

We now describe key diagnostics of the resulting MSCM geomagnetic model. First, we quantify the fit of the model to the data, and then we present spatial and temporal power spectra. Finally, we show the time-dependent part of the model on the core and Earth's surface in Section 4.3.

4.1 Fit to Satellite Data

We begin by reporting the fit of the MSCM to its satellite data sources. Weighted residual statistics for CSES, MSS-1, and Swarm A, B, and C are provided in Tables 1 to 3, respectively. Each table shows the number of satellite data points (Ndata), the Huber weighted mean residual (Mean), and the Huber weighted root mean square (RMS) residual, each of which is normalized by the sum of the Huber weights. A nonzero mean residual indicates a biased unmodeled signal, whereas a large RMS value indicates a significant difference between the model and the data. We show the individual vector components, and we separate the scalar components into polar and nonpolar (see Section 2.4).

Our Swarm residuals (Table 3) are 3–6 nT, which are comparable to (but slightly higher than) those reported by CHAOS-7 of 2–3 nT (Finlay et al., 2020). Of particular note is that the residuals have a low mean, indicating unbiased noise in the Swarm data. Discrepancies between the MSCM and CHAOS-7 may result from not fully accounting for the effects of ionospheric currents, tidal constituents, and the treatment of induced fields. Despite our larger data residuals compared with CHAOS-7, the MSCM residuals remain approximately 0.01% of the maximum field strength at satellite altitude.

Table 1. Model statistics of the misfit between MSCM and CSES data.

Component	CSES		
	Ndata	Mean	RMS
F_{polar} (nT)	40,993	1.47	2.76
F_{nonpolar} (nT)	42,512	0.02	3.60
B_r (nT)	42,512	−0.41	8.42
B_θ (nT)	42,512	−2.05	5.81
B_ϕ (nT)	42,512	0.55	8.99

Table 2. Model statistics of the misfit between MSCM and MSS-1 data.

Component	MSS-1		
	Ndata	Mean	RMS
F_{nonpolar} (nT)	106,660	0.65	4.65
B_r (nT)	106,660	0.05	3.32
B_θ (nT)	106,660	−0.52	5.90
B_ϕ (nT)	106,660	−0.13	5.00

Table 3. Model statistics of misfit between MSCM and Swarm data.

Component	Swarm-A			Swarm-B			Swarm-C		
	Ndata	Mean	RMS	Ndata	Mean	RMS	Ndata	Mean	RMS
F_{polar} (nT)	153,505	−0.88	5.79	151,210	−0.84	5.55	13,598	−0.78	4.88
$F_{nonpolar}$ (nT)	588,720	−0.08	3.99	579,660	0.01	3.98	49,964	0.00	3.55
B_r (nT)	588,720	−0.10	2.80	579,660	0.08	2.76	49,964	0.13	2.64
B_θ (nT)	588,720	0.13	5.43	579,660	0.33	5.49	49,964	0.14	5.02
B_ϕ (nT)	588,720	−0.15	4.75	579,660	−0.06	4.80	49,964	−0.33	4.39

Table 2 shows slightly larger diagnostics for MSS-1, which confirms the comparable data quality of the MSS-1 mission and the Swarm mission (Jiang Y et al., 2024). In comparison, the CSES vector components (Table 1) are either biased and have a moderate RMS (6 nT for B_θ) or are unbiased and have a large RMS (8–9 nT for B_r, B_ϕ). Both polar and nonpolar CSES scalar data have an RMS smaller than the equivalent data from Swarm, but the polar data show biased noise. Overall, the best fitting CSES data are the nonpolar scalar data (QD latitude ≤20°). Figure 3 shows information similar to that contained in the tables but as histograms of unweighted residuals. Overall, the residuals for Swarm A, B, and C exhibit narrow, near-zero-centered peaks with B_r and the magnetic intensity (F) showing the smallest residuals. This result highlights the high quality and low noise levels of the Swarm datasets. The MSS-1 residuals are slightly broader than those of the Swarm satellites and show the smallest residuals for B_r. In contrast, the residuals for CSES display significantly broader peaks, indicating higher noise levels in the data. Notably, the residuals of B_r and B_ϕ in our model compared with CSES data lack sharp peaks and exhibit a very large spread. This is likely due to issues with the mechanical link between the FGM and the star tracker on the CSES, which have already been documented (Yang YY et al., 2021a).

We now turn to the mutual consistency of the data from each satellite. The reweighted Huber scheme, at each iteration, downweights any data that have a residual exceeding 1.5 times the overall RMS misfit, giving higher value weights to data that are consistent with the model. This means that the data are, in effect, self-selecting: if there are few poor-quality data points (with greater noise), these will be downweighted compared with the majority of higher quality data that define the model. This step allows us to examine the mutual data quality among the three different missions. We quantify the final data weights in Figure 4, which illustrates the monthly average Huber weights for vector and scalar data from each satellite. We note for comparison that if all data were the same quality, the Huber weights would be uniform.

The Huber weights for each data type are all time dependent, showing variations on monthly timescales. The magnitudes of the variations are typically up to 10% of the signal. The weights appear to follow the temporal distribution of the data counts (Figure 2), with a significant downweighting of Swarm component weights in July–August 2023, particularly in the B_ϕ components, which align with the period of Swarm data sparsity (see earlier discussion about Swarm data in Section 2.1). Overall, B_θ and F_{polar}

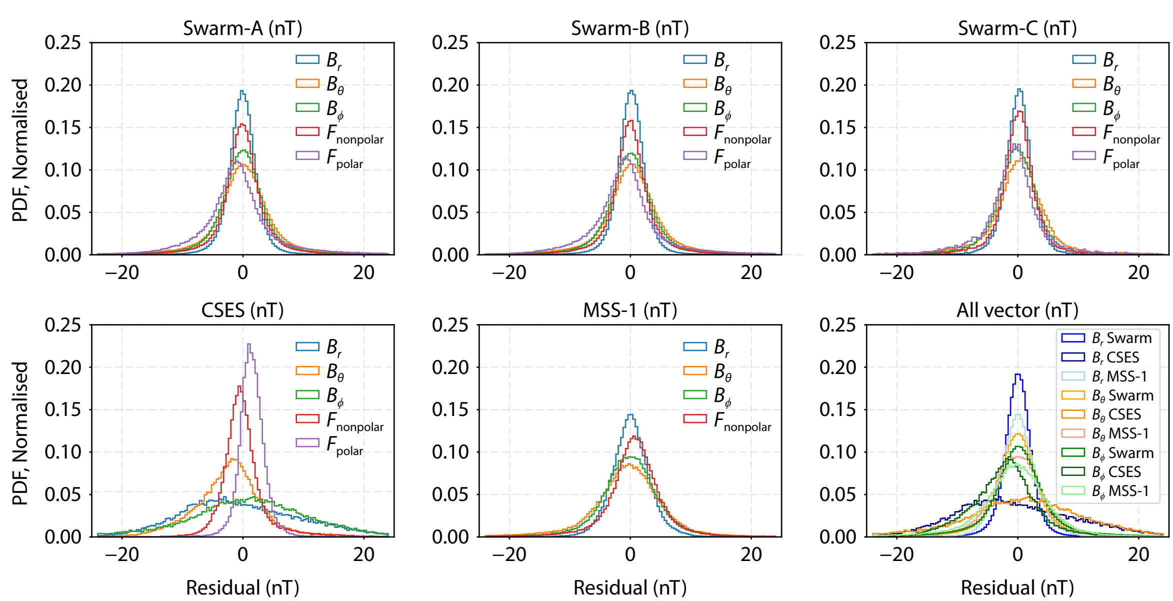

Figure 3. Histograms of the unweighted residuals between the MSCM and each satellite. Blue represents radial component differences, orange represents north–south component differences, green represents east–west component differences, red represents nonpolar scalar data differences, and purple represents polar scalar differences.

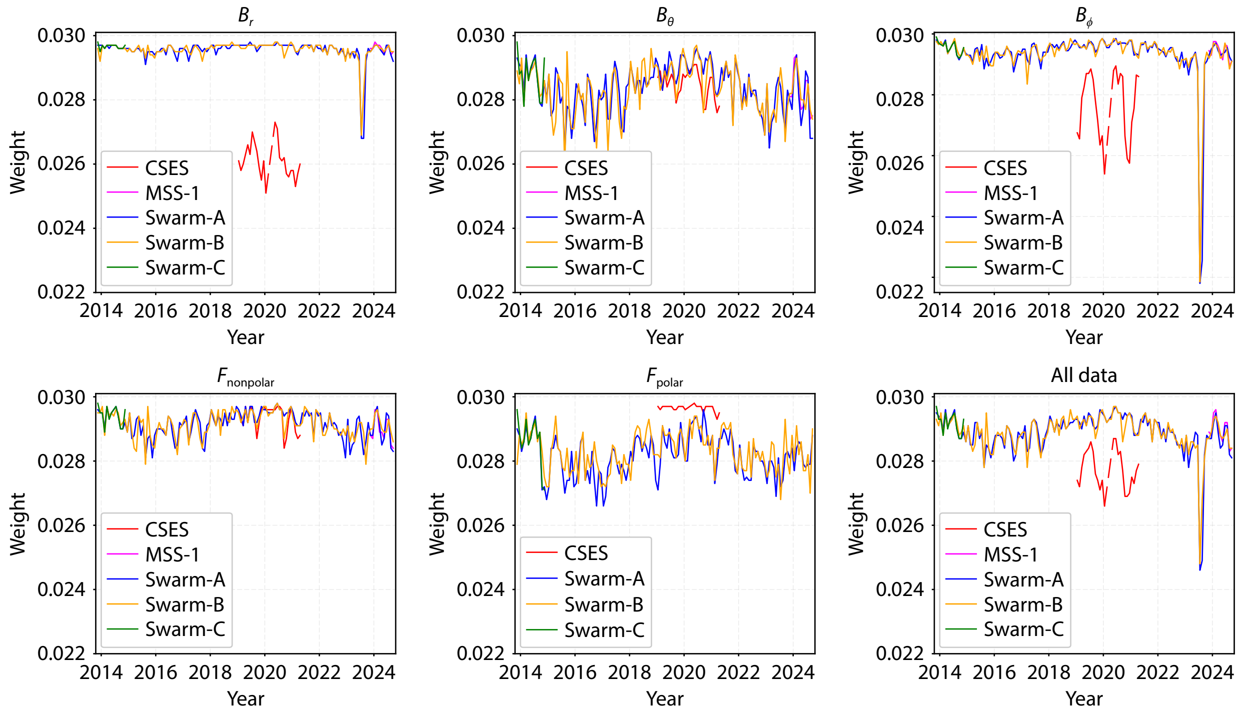

Figure 4. Monthly average data weights for each satellite dataset. The dashed red line indicates the period between February and April 2020 during which CSES data were unavailable.

are the most downweighted of the data.

In terms of the different geomagnetic missions, the weights for Swarm A, B, and C and MSS-1 are comparable at all times. In comparison, the weights for B_r and B_ϕ of CSES data are 15%–20% lower than those of the other satellites, consistent with their large RMS residuals in Table 1. Finally, the weight of F_{polar} for CSES is higher than those of the Swarm satellites, indicating higher data quality. However, it is important to note that the CSES data cover only regions between 20° QD latitude and 65° geographic latitude in the northern hemisphere, and between −20° QD latitude and −65° geographic latitude in the southern hemisphere. In high-latitude regions, particularly in the polar areas, modeling the Earth's magnetic field becomes more complex because of external fields, such as field-aligned currents. The higher weight of the CSES scalar data compared with Swarm data is likely more a reflection of the different definitions of "polar" data than instrumentation accuracy. Because CSES polar data do not extend as far north as those from Swarm, the CSES polar data contain a weaker unmodeled external signal compared with Swarm data, leading to higher weights.

4.2 Spectra of the Internal Field

The Lowes–Mauersberger spectra (Mauersberger, 1956; Lowes, 1966) of the core and lithospheric fields at 2024.0 from the MSCM, CHAOS-7, CHAOS-8, and MIFM models are shown in Figure 5, with the MSCM model represented in black. All models show very similar spectra up to degree 40. The figure also shows spectra of the differences between the models and highlights in particular the close agreement across all degrees between the MSCM and CHAOS-7 models, and between the MSCM and CHAOS-8 models. The coefficients of the CHAOS-7 and CHAOS-8 models are identical

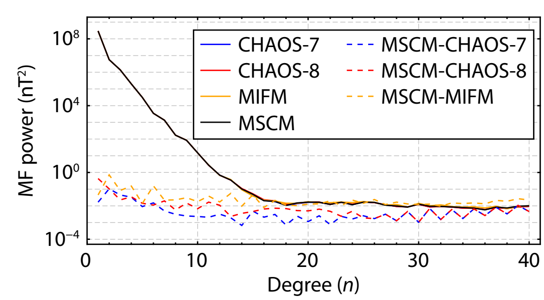

Figure 5. Lowes–Mauersberger spectra of a variety of models and their differences for degrees n = 1–40 at epoch 2024.0 for the magnetic field (MF).

for degrees ≥26 (static lithospheric field), which explains the overlap of the blue and red dashed lines (Figure 5).

Figure 6 presents Lowes–Mauersberger spectra for the first time derivative of the internal field (SV) at epochs 2015.0, 2020.0, and 2024.0. At all epochs, the MSCM demonstrates a high level of consistency in large-scale SV features compared with all models shown. The figure also shows that the SV spectra of the model differences between the MSCM and CHAOS-7/CHAOS-8 models are small (<1%) compared with the spectra of the SV itself, particularly for degrees $n \leq 10$, for all times shown. In 2020.0, the SV difference between the MSCM and CGGM is noticeably higher than the difference with the CHAOS models. This result might be expected because the CGGM is based on poor-quality data over a short period of time (from March 3, 2018, to September 20, 2019). In 2024.0, there is a relatively large difference between degrees 5 and 8 between the MSCM and MIFM compared with the MSCM and CHAOS models. This is likely due to the lack of temporal regu-

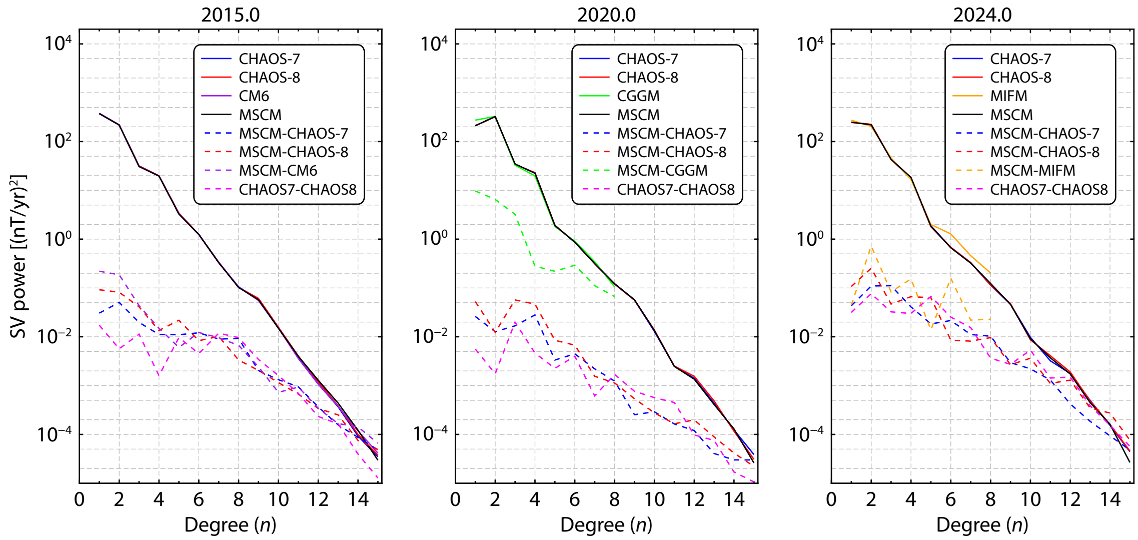

Figure 6. Lowes–Mauersberger spectra of the SV (n = 1–15) from various models (solid lines) and their differences from the MSCM (dashed lines) at the Earth's surface at epochs 2015.0 (left), 2020 (middle), and 2024.0 (right).

larization applied in the MIFM.

4.3 Core Fields in 2024

Figures 7 and 8 present maps of the core radial magnetic field, SV, and secular acceleration (SA) derived from the MSCM and their differences with CHAOS-7 and CHAOS-8 at epoch 2024.0, at both the Earth's surface and the core–mantle boundary (CMB). To maintain consistency, all models are truncated at degree 15. At the Earth's surface, the core field from the MSCM agrees well with that from the CHAOS models, with a difference of 0.02%. This relative difference increases with the increasing time derivative, with the SA differing by up to 50%, a reflection of the challenges in constraining the SA through any geomagnetic field model (Gillet et al., 2010; Lesur et al., 2022). The comparison for the CMB shows similar trends but with higher amplitudes because of being closer to the internal source.

At the Earth's surface, regions such as the western Pacific, northeast of Australia, and parts of the Southern Ocean display increasingly positive SA, whereas the central Pacific (near Hawaii) and parts of the North Atlantic exhibit negative SA. In the map of SV, the strongest features are in the south Atlantic, close to the SAA. At the CMB, the SV reveals intense structures at high latitudes beneath the Bering Strait and northeastern Siberia, along with strong patches of alternate signs in the equatorial Atlantic region, which are comparable to those observed in the CHAOS models. The difference maps reveal strong zonal structures, which may stem from differences in how induction signals are modeled (Sabaka et al., 2020). The CHAOS-7 incorporates an induction field, whereas the CHAOS-8 also includes ionospheric currents and their associated induction potentials. In contrast, the MSCM does not account for ionospheric effects and the associated induction.

5. South Atlantic Anomaly

We now turn to how our model describes the SAA, the region characterized by a weakened magnetic intensity extending across eastern Africa, the Atlantic Ocean, and South America (Nasuddin et al., 2019). Within the SAA, low Earth orbit satellites are at risk of damage, and astronauts face increased radiation exposure when passing through this region (Heirtzler, 2002). Over the past two centuries, a decay in the geomagnetic axial dipole has been observed, and it is anticipated that this weak-intensity region will continue to expand and shift westward over time (Aubert, 2015; Yi SQ et al., 2023).

Figures 9a–9d show the total intensity of the surface geomagnetic field for 2015, 2020, and 2024, and the difference in intensity between 2024 and 2015, respectively. The SAA, prominently depicted in blue, stands out as the region with the weakest magnetic field strength, with an overall (principal) minimum at approximately (25°S, 60°W). Figure 9 illustrates that the magnetic field strength in the SAA region has decreased from 2015 to 2024, accompanied by an expansion of the area of the region, as seen, for example, in the monotonic growth of the area enclosed by the 22,500 nT contour line close to its overall minimum. In 2020, a distinct secondary minimum emerged at approximately 0° longitude and 40°S latitude, first reported when using the CHAOS-7 model (Finlay et al., 2020). Figure 9d shows that the SAA principal minimum lies within a region of field intensity that has changed by 290 nT over the period of 2015 to 2024. The secondary minimum, although a smaller feature, lies within the eastern SAA region showing larger intensity changes of 730 nT, approximately 2.5 times greater than that of the principal minimum. We note that the greatest absolute changes in intensity do not occur within the SAA, but north of it (over North America) and east of it (over the South Indian Ocean). It is also striking that the global change in intensity is mostly hemispheric: negative between 180°W and 0°W, and positive between 0°E and 180°E.

In Figure 10, we examine the changes in both the principal and secondary intensity minima within the SAA over time. For the years 2015.0, 2020.0, and 2024.0, we show the profile of the field intensity along the great circle that connects both minima in 2020. For this comparison, we use the same great circle for all times, even though the minima change very slightly in position

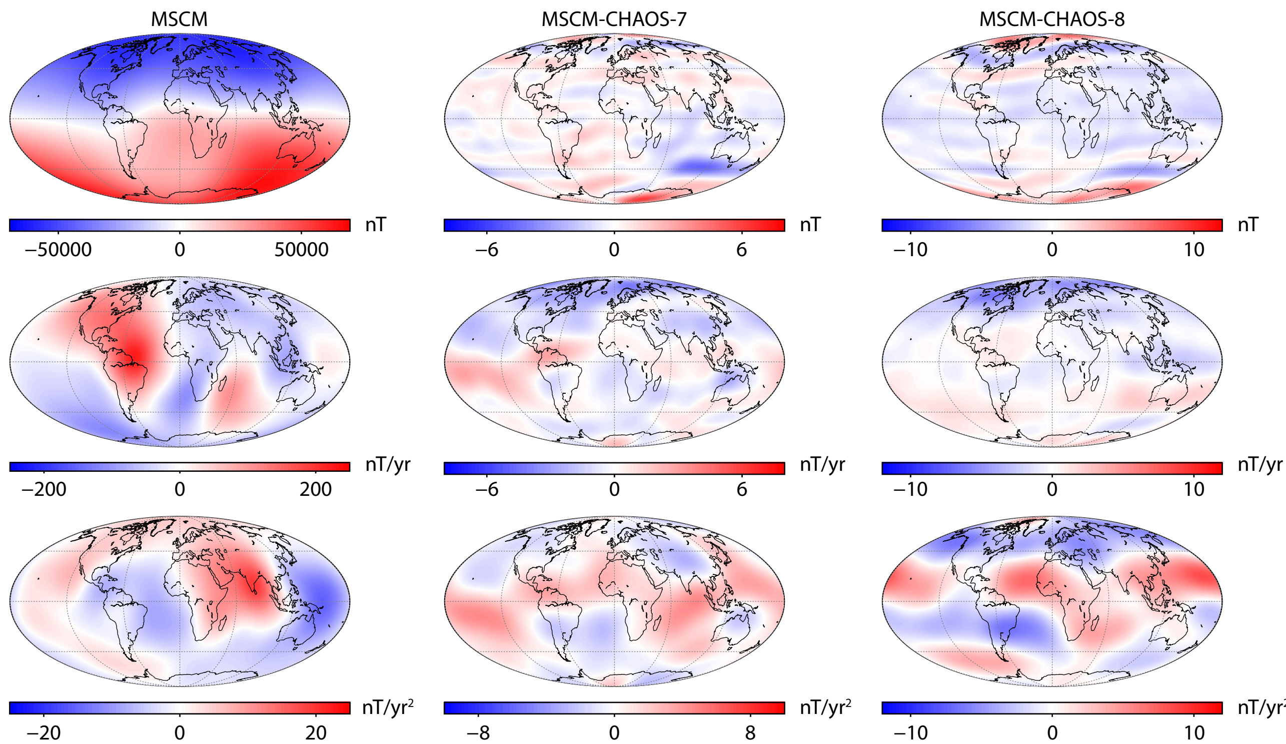

Figure 7. At epoch 2024.0, evaluated at the Earth's surface (up to degree 15), the core radial magnetic field (top), its first time derivative (SV, middle row), and its second time derivative (SA, bottom row) from the MSCM (left) and from the MSCM minus CHAOS-7 (middle) and CHAOS-8 (right).

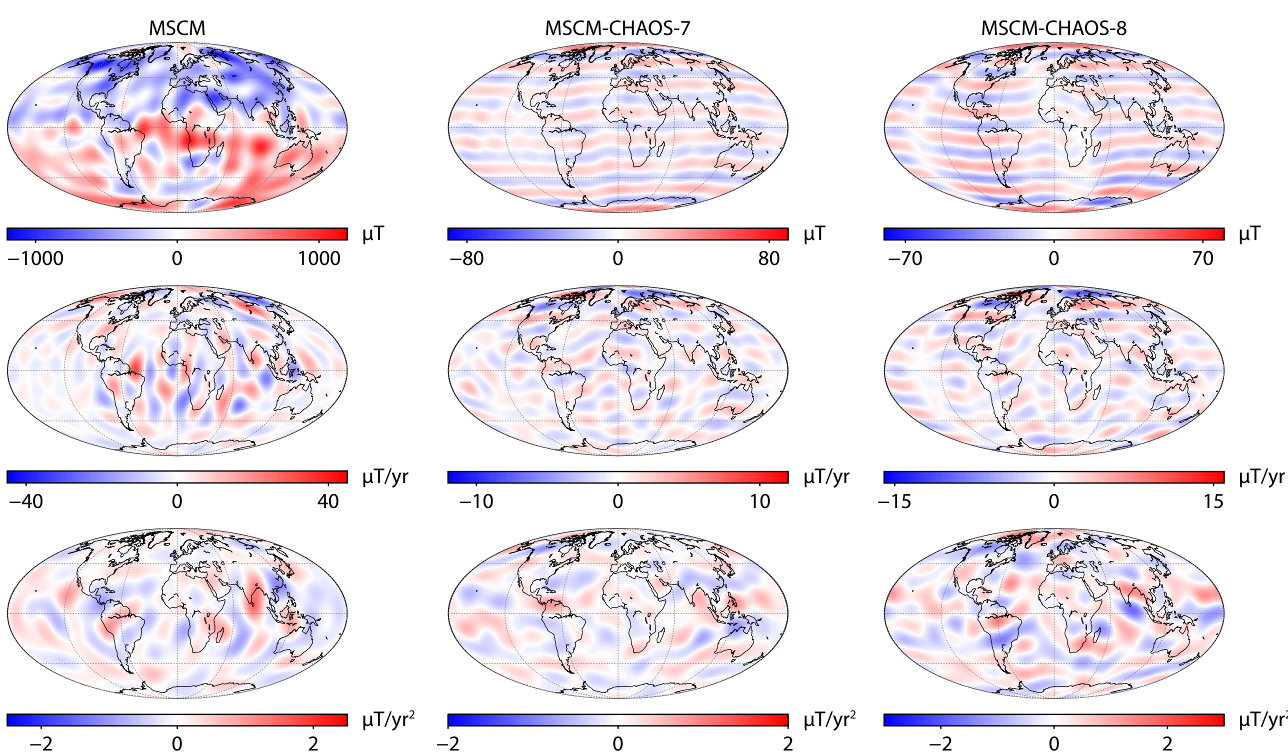

Figure 8. At epoch 2024.0, evaluated at the CMB (up to degree 15), the core radial magnetic field (top), its first time derivative (SV, middle row), and its second time derivative (SA, bottom row) from the MSCM (left) and from the MSCM minus CHAOS-7 (middle) and CHAOS-8 (right).

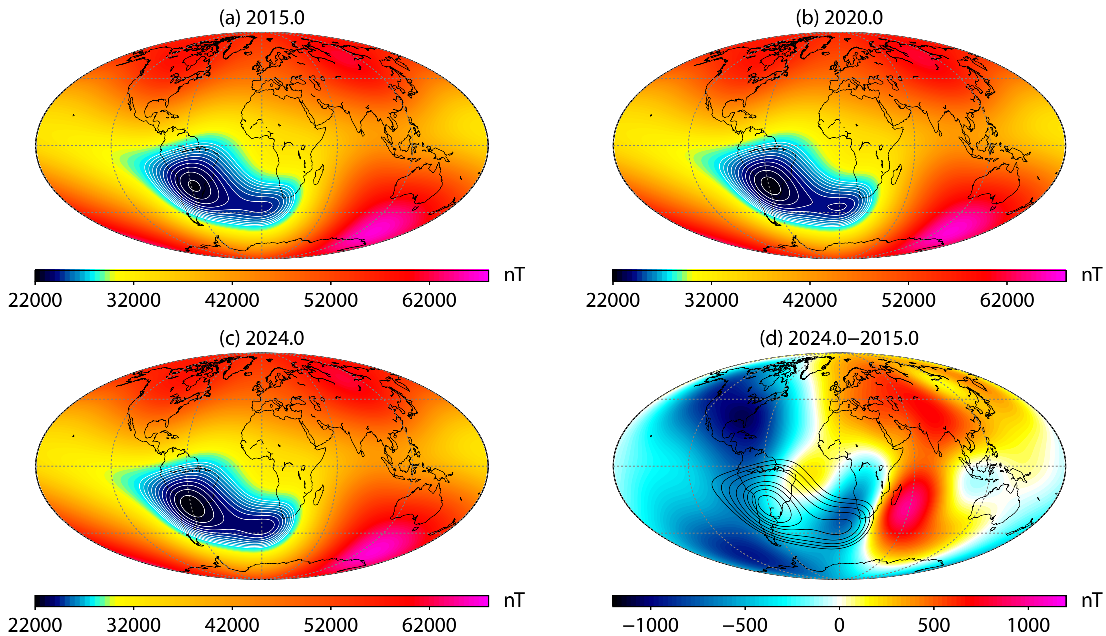

Figure 9. Field intensity at the Earth's surface in (a) 2015, (b) 2020, and (c) 2024, and (d) intensity difference between 2024 and 2015, highlighting changes in the SAA. The contour lines (white) are plotted every 500 nT between 22,000 to 28,000. In (d), the contour lines are taken from (c) for reference.

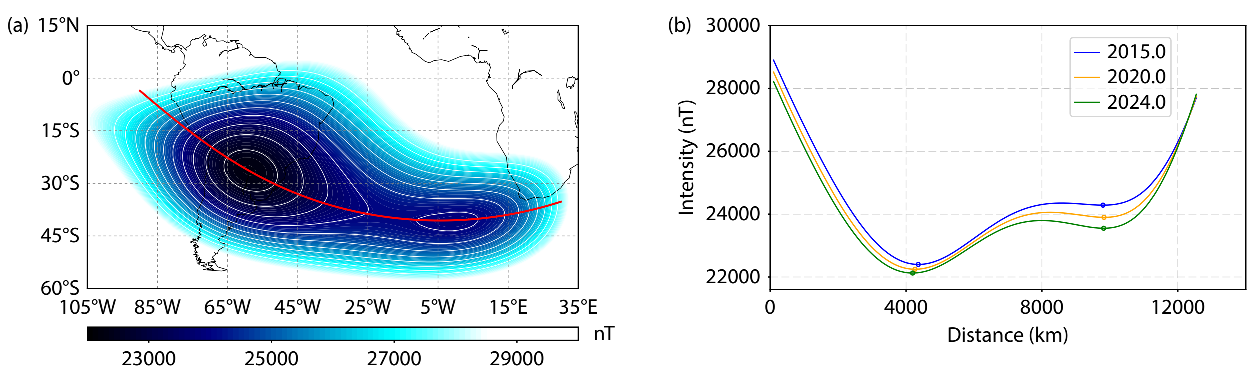

Figure 10. The 2020 geomagnetic field intensity of the SAA (left) with a red line marking a great circle through the two minimum intensity points, and the intensity profile along this circle (right) illustrating variations with distance for 2015.0 (blue line), 2020.0 (orange line), and 2024.0 (green line). The principal and secondary minima are marked by small colored circles (right) for each epoch shown.

(Figure 10a). Figure 10b shows the persistence of the secondary minimum throughout the entire time period. The absence of the secondary minima in the white contours of Figures 9a and 9c is caused only by the choice of contour level. Between 2015 and 2024, from approximately 90°W to 50°W (distance 0 to 5000 km), the three curves indicate a gradual decline in magnetic field intensity over time, accompanied by a noticeable westward shift of the principal minimum. Over the 9 years of our model, this minimum has moved westward a distance of approximately 165 km, at an average speed of approximately 20 km per year, similar to the typical westward drift speed (Dumberry and Finlay, 2007; Rogers et al., 2025). The western edge of the SAA also moves westward at a similar rate. A greater change in the intensity is identified for the secondary minimum at approximately 20°W to 35°W (a distance of 8000 to 12,000 km), where the three curves indicate a relatively large drop in intensity. In contrast to the principal minimum, this secondary minimum does not appear to move westward, instead decreasing in intensity *in situ*. This distinct behavior is also consistent with the eastern edge of the SAA at 12,000 km (approximately 23°E to 30°E), where the intensity remains relatively stable with the three curves closely aligned.

A main finding from our model is that the time dependence of the SAA appears to be split into two. The principal minimum on the western side is deepening slowly while moving westward. Meanwhile, the secondary minimum is decreasing in intensity more rapidly but remaining *in situ*. This finding is supported by CHAOS-7 (Figure 16 in Finlay et al., 2020), which shows a field intensity difference similar to our Figure 9d. Their contours of intensity overlap with the 0 nT intensity change on the eastern edge of the SAA and overlap with the nonzero (negative) intensity change on the western edge. This characteristic therefore seems to be independent of the model and persistent over the last decade. Whether a different mechanism for the intensity decrease operates to the east and west of the SAA needs to be explored further. Nevertheless, this could have implications for the long-lived nature of the SAA (Nilsson et al., 2022; Engbers et al., 2024) and spacecraft passing through this region (Heirtzler, 2002).

To investigate the cause of any change to the SAA, we would like to link the core field evolution to the structure of the SAA. It is important to remember that features on the CMB are smeared as the field is upward continued to the Earth's surface, represented formally by averaging kernels or Green's functions (Gubbins and Roberts, 1983). Therefore, the linearized sensitivity of the SAA is not linked to specific features on the CMB but are instead averages over the CMB. The Green's functions were reported by Finlay et al. (2020) for the two minima of the SAA, which showed the underlying importance of time-dependent reversed flux patches. It is important to note that these Green's functions had maximum sensitivity almost directly underneath the two SAA minima, showing their dependence on only local features.

In view of better understanding the evolving SAA, it is of interest to explore the time dependence of the core field directly beneath the SAA at the CMB. We focus only on changes underneath the principal SAA minimum. Accordingly, Figures 11 and 12 show a comparison of time–longitude and time–latitude maps of the

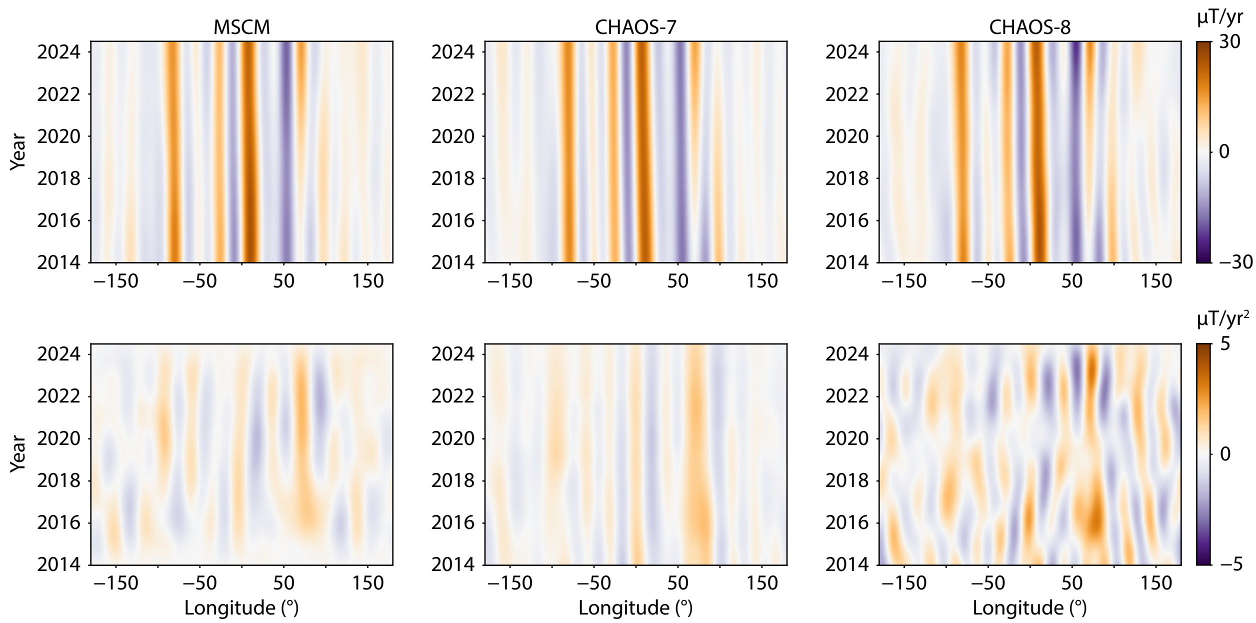

Figure 11. Time–longitude diagrams of radial SV (top) and SA (bottom) along latitude 25°S at the CMB for the MSCM (left), CHAOS-7 (middle), and CHAOS-8 (right) models.

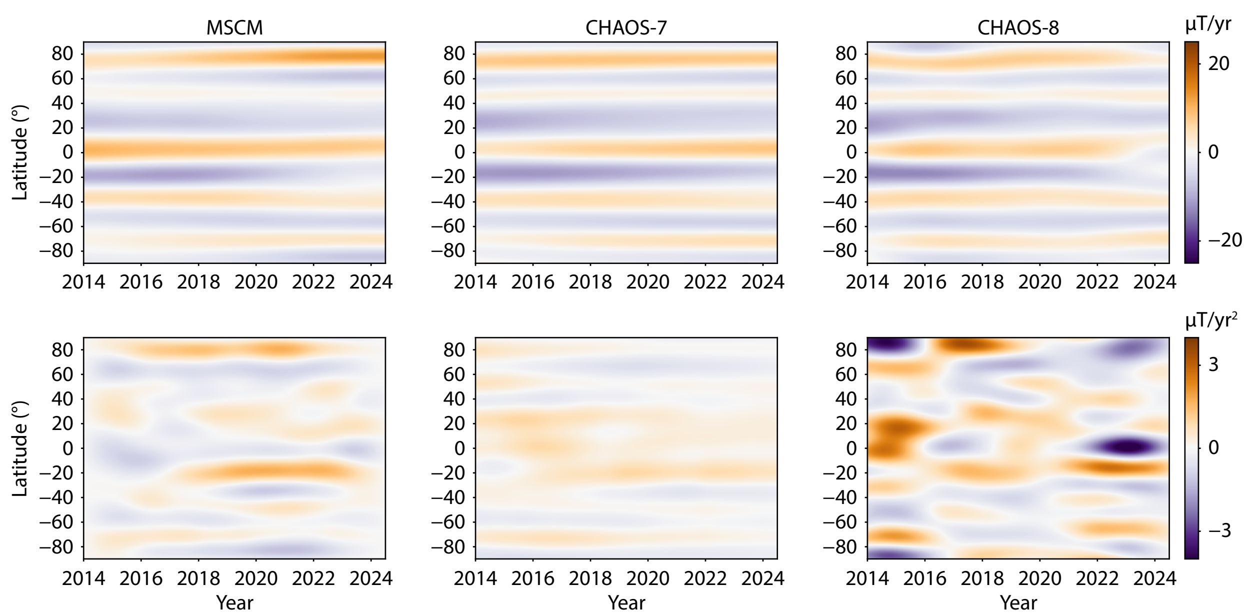

Figure 12. Time–latitude diagrams of radial SV (top) and SA (bottom) along the longitude 60°W at the CMB for the MSCM (left), CHAOS-7 (middle), and CHAOS-8 (right) models.

CMB radial SV and SA centered at 25°S, 60°W with the MSCM (left), CHAOS-7 (center), and CHAOS-8 (right)

Overall, the MSCM SV closely aligns with the CHAOS-7 and CHAOS-8 SV. In particular, all models show persistent features in the SV, which present as stripes (either vertical or horizontal, respectively), although there is evidence of change on decadal timescales. There is a greater difference between the models in the SA. Although all models show similar stripe-like features, there is significant spatiotemporal variability. The CHAOS-8 has the highest amplitudes and more structure indicating rapidly changing SA. The CHAOS-7 has the lowest amplitudes and its SA changes most slowly (of the models compared) over time. The MSCM lies in between the CHAOS-7 and CHAOS-8 models in terms of amplitude and variability. Each of the three models fits the data reasonably but makes different choices regarding data sources and regularization. This figure shows the challenges in uniquely identifying the SA on the core surface (Lesur et al., 2022).

Regarding the SAA, the changes we observed over the period from 2015 to 2024 are likely not caused by significant changes in the core field on the CMB because of the persistence of features in the SV over the same timescale. Instead, the cumulative average of possibly multiple small changes in both amplitude and structure over this timescale produces the changes identified in the SAA (Finlay et al., 2020).

6. Conclusions

In this article, we present the MSCM geomagnetic field model, which incorporates vector and scalar data from the Swarm A, Swarm B, Swarm C, CSES, and MSS-1 satellites. It accounts for the time-varying core magnetic field, lithospheric magnetic field, and magnetospheric field, covering a time span from 2014.0 to 2024.5. We use the MSCM to analyze decadal variations in the Earth's magnetic field, including changes to the SAA.

The MSCM integrates both vector and scalar data from the Swarm, CSES, and MSS-1 spacecraft, exploring for the first time the potential of combining CSES vector data with other data sources to develop a global model. Although our results indicate that CSES scalar data are comparable in quality to Swarm scalar data, the CSES vector data, in particular the radial and the azimuthal components, contain significant unmodeled signals leading to relatively high residuals and associated low weighting. Despite this issue, we successfully constructed a large-scale geomagnetic field model utilizing CSES vector data, extending the CGGM (Yang YY et al., 2021a) to include other data. Additionally, with the MSCM, we show that MSS-1 data — notably, both vector and scalar data from the MSS-1 — can be successfully incorporated into our fully time-dependent smoothed geomagnetic field model and are of high quality, comparable to those of Swarm A, B, and C. Our modeling strategy was to create a hybrid of CHAOS-7 and CHAOS-8: we used a regularization similar to that of CHAOS-7 but applied it to a dataset most similar to the satellite data used in CHAOS-8 (because of the inclusion of MSS-1 data). Our model shows geomagnetic field behavior that is intermediate between the CHAOS-7 and CHAOS-8 models.

Using the MSCM, we report the newly identified time-dependence of the SAA. In particular, we found that, behaviorally, the SAA appears to be split into two: the western part shows a modest intensity drop and westward drift, whereas the secondary minimum in the eastern part shows a significant intensity drop (2.5 times larger) and no drift. These features have been constrained in part by data from the MSS-1, whose equatorial orbit will continue to provide coverage of the SAA in the coming years.

Acknowledgments

We thank Clemens Kloss at Danmarks Tekniske Universitet (DTU) for his guidance in data processing and regularization, and Chris Finlay at DTU for discussions based on an early version of the work. This work was supported by the National Natural Science Foundation of China (Grant No. 42274003). PWL was supported by Swarm DISC (Swarm Data, Innovation, and Science Cluster), funded by the European Space Agency (ESA; Contract No. 4000109587). HFR acknowledges funding from the UK Natural Environment Research Council (Grant No. NE/V010867/1). The numerical calculations in this article were performed at the Supercomputing Center of Wuhan University.

Data Availability Statement

The Swarm data are available at https://earth.esa.int/eogateway/missions/swarm/data. The CSES data are available at https://www.leos.ac.cn/#/home. The MSS-1 data used in the study are available at https://mss.must.edu.mo/data.html. The CHAOS-7 model can be accessed at https://www.spacecenter.dk/files/magnetic-models/CHAOS-7/. The CHAOS-8 model can be accessed at https://www.spacecenter.dk/files/magnetic-models/CHAOS-8/index.html. The CM-6 model can be accessed at https://www.spacecenter.dk/files/magnetic-models/CM6/. The CGGM can be accessed at https://www.leos.ac.cn/#/article/info/237. MSCM model can be accessed at https://github.com/YuGaoGeomag/MSCM.

References

Alken, P., Thébault, E., Beggan, C. D., Aubert, J., Baerenzung, J., Brown, W. J., Califf, S., Chulliat, A., Cox, G. A., … Wardinski, I. (2021). Evaluation of candidate models for the 13th generation International Geomagnetic Reference Field. *Earth, Planets Space, 73*(1), 48. https://doi.org/10.1186/s40623-020-01281-4

Amit, H., Terra-Nova, F., Lézin, M., and Trindade, R. I. (2021). Non-monotonic growth and motion of the South Atlantic Anomaly. *Earth, Planets Space, 73*(1), 38. https://doi.org/10.1186/s40623-021-01356-w

Aubert, J. (2015). Geomagnetic forecasts driven by thermal wind dynamics in the Earth's core. *Geophys. J. Int.*, *203*(3), 1738–1751. https://doi.org/10.1093/gji/ggv394

Baerenzung, J., Holschneider, M., Saynisch-Wagner, J., and Thomas, M. (2022). Kalmag: A high spatio-temporal model of the geomagnetic field. *Earth, Planets Space, 74*(1), 139. https://doi.org/10.1186/s40623-022-01692-5

Constable, C., and Constable, S. (2023). A grand spectrum of the geomagnetic field. *Phys. Earth Planet. Inter.*, *344*, 107090. https://doi.org/10.1016/j.pepi.2023.107090

Constable, C. G. (1988). Parameter estimation in non-Gaussian noise. *Geophys. J. Int.*, *94*(1), 131–142. https://doi.org/10.1111/j.1365-246X.1988.tb03433.x

De Boor, C. (1978). *A Practical Guide to Splines*. New York: Springer.

Domingos, J., Jault, D., Pais, M. A., and Mandea, M. (2017). The South Atlantic Anomaly throughout the solar cycle. *Earth Planet. Sci. Lett.*, *473*, 154–163. https://doi.org/10.1016/j.epsl.2017.06.004

Dumberry, M., and Finlay, C. C. (2007). Eastward and westward drift of the

Earth's magnetic field for the last three millennia. *Earth Planet. Sci. Lett.*, *254*(1-2), 146–157. https://doi.org/10.1016/j.epsl.2006.11.026

Engbers, Y. A., Holme, R., and Biggin, A. J. (2024). Miocene time-averaged geomagnetic field model suggests long lived mantle control and recurring structure in the South Atlantic. *Earth Planet. Sci. Lett.*, *626*, 118535. https://doi.org/10.1016/j.epsl.2023.118535

Finlay, C. C., Gillet, N., Aubert, J., Livermore, P. W., and Jault, D. (2023). Gyres, jets and waves in the Earth's core. *Nat. Rev. Earth Environ.*, *4*(6), 377–392. https://doi.org/10.1038/s43017-023-00425-w

Finlay, C. C., Kloss, C., Olsen, N., Hammer, M. D., Tøffner-Clausen, L., Grayver, A., and Kuvshinov, A. (2020). The CHAOS-7 geomagnetic field model and observed changes in the South Atlantic Anomaly. *Earth Planets Space*, *72*(1), 156. https://doi.org/10.1186/s40623-020-01252-9

Gillet, N., Lesur, V., and Olsen, N. (2010). Geomagnetic core field secular variation models. *Space Sci. Rev.*, *155*(1), 129–145. https://doi.org/10.1007/s11214-009-9586-6

Gubbins, D., and Roberts, N. (1983). Use of the frozen flux approximation in the interpretation of archaeomagnetic and palaeomagnetic data. *Geophys. J. Int.*, *73*(3), 675–687. https://doi.org/10.1111/j.1365-246X.1983.tb03339.x

Heirtzler, J. R. (2002). The future of the South Atlantic anomaly and implications for radiation damage in space. *J. Atmos. Solar-Terr. Phys.*, *64*(16), 1701–1708. https://doi.org/10.1016/S1364-6826(02)00120-7

Holme, R., and Bloxham, J. (1996). The treatment of attitude errors in satellite geomagnetic data. *Phys. Earth Planet. Inter.*, *98*(3-4), 221–233. https://doi.org/10.1016/S0031-9201(96)03189-5

Hulot, G., Finlay, C. C., Constable, C. G., Olsen, N., and Mandea, M. (2010). The magnetic field of planet earth. *Space Sci. Rev.*, *152*(1), 159–222. https://doi.org/10.1007/s11214-010-9644-0

Jiang, Y., Finlay, C. C., Olsen, N., Tøffner-Clausen, L., Yan, Q., and Zhang, K. K. (2024). Macau Scientific Satellite-1 initial magnetic field model. *Geophys. Res. Lett.*, *51*(22), e2024GL112305. https://doi.org/10.1029/2024GL112305

Kakad, A., and Kakad, B. (2022). An audit of geomagnetic field in polar and South Atlantic Anomaly regions over two centuries. *Adv. Space Res.*, *69*(5), 2142–2157. https://doi.org/10.1016/j.asr.2021.12.011

Kloss, C. (2021). *Geomagnetic Field Modelling and Polar Ionospheric Currents*. Lyngby: Technical University of Denmark.

Kloss, C., Finlay, C. C., Olsen, N., Tøffner-Clausen, L., Gillet, N., and Grayver, A. (2024). The DTU geomagnetic field parent model and derived IGRF-14 candidate models.

Lesur, V., Gillet, N., Hammer, M. D., and Mandea, M. (2022). Rapid variations of Earth's core magnetic field. *Surv. Geophys.*, *43*(1), 41–69. https://doi.org/10.1007/s10712-021-09662-4

Livermore, P., Brown, W., Beggan, C., and Gubbins, D. (2024). Geomagnetic twin satellites MSS-1: Progress and future plans. *Astron. Geophys.*, *65*(1), 1.33–1.37. https://doi.org/10.1093/astrogeo/atae009

Lowes, F. J. (1966). Mean-square values on sphere of spherical harmonic vector fields. *J. Geophys. Res.*, *71*(8), 2179–2179. https://doi.org/10.1029/JZ071i008p02179

Mauersberger, P. (1956). Das Mittel der Energiedichte des geomagnetischen Hauptfeldes an der Erdoberfläche und seine säkulare Änderung. *Gerl. Beitr. Geophys.*, *65*, 207–215.

Nasuddin, K. A., Abdullah, M., and Abdul Hamid, N. S. (2019). Characterization of the South Atlantic Anomaly. *Nonlinear Processes Geophys.*, *26*(1), 25–35. https://doi.org/10.5194/npg-26-25-2019

Neubert, T., Mandea, M., Hulot, G., Von Frese, R., Primdahl, F., Jørgensen, J. L., Friis-Christensen, E., Stauning, P., Olsen, N., and Risbo, T. (2001). Ørsted satellite captures high-precision geomagnetic field data. *Eos, Trans. Am. Geophys. Union*, *82*(7), 81–88. https://doi.org/10.1029/01eo00043

Nilsson, A., Suttie, N., Stoner, J. S., and Muscheler, R. (2022). Recurrent ancient geomagnetic field anomalies shed light on future evolution of the South Atlantic Anomaly. *Proc. Natl. Acad. Sci. USA*, *119*(24), e2200749119. https://doi.org/10.1073/pnas.2200749119

Olsen, N., Friis-Christensen, E., Floberghagen, R., Alken, P., Beggan, C. D., Chulliat, A., Doornbos, E., da Encarnação, J. T., Hamilton, B., … Visser, P. N. (2013). The *Swarm* Satellite Constellation Application and Research Facility (SCARF) and *Swarm* data products. *Earth, Planets Space*, *65*(11), 1189–1200. https://doi.org/10.5047/eps.2013.07.001

Olsen, N., Lühr, H., Finlay, C. C., Sabaka, T. J., Michaelis, I., Rauberg, J., and Tøffner-Clausen, L. (2014). The CHAOS-4 geomagnetic field model. *Geophys. J. Int.*, *197*(2), 815–827. https://doi.org/10.1093/gji/ggu033

Richmond, A. D. (1995). Ionospheric electrodynamics using magnetic apex coordinates. *J. Geomag. Geoelec.*, *47*(2), 191–212. https://doi.org/10.5636/jgg.47.191

Rogers, H. F., Gillet, N., Aubert, J., Personnettaz, P., Mandea, M. (2025). Effects of geodynamo priors and geomagnetic data on inverted core surface flows. *Phys. Earth Planet. Inter.*, 107323. https://doi.org/10.1016/j.pepi.2025.107323.

Rygaard-Hjalsted, C., Mosegaard, K., and Olsen, N. (2000). Resolution studies of fluid flow models near the core–mantle boundary using Bayesian inversion. In P. C. Hansen, et al. (Eds.), *Methods and Applications of Inversion* (pp. 255–275). Berlin: Springer. https://doi.org/10.1007/BFb0010296

Sabaka, T. J., Olsen, N., Tyler, R. H., and Kuvshinov, A. (2015). CM5, a pre-Swarm comprehensive geomagnetic field model derived from over 12 yr of CHAMP, Ørsted, SAC-C and observatory data. *Geophys. J. Int.*, *200*(3), 1596–1626. https://doi.org/10.1093/gji/ggu493

Sabaka, T. J., Tøffner-Clausen, L., Olsen, N., and Finlay, C. C. (2020). CM6: A comprehensive geomagnetic field model derived from both CHAMP and Swarm satellite observations. *Earth Planets Space*, *72*(1), 80. https://doi.org/10.1186/s40623-020-01210-5

Stevanović, Đ., Comparetti, N., Mazzocato, M. (2023). *Swarm DISC Weekly Report*. Serco S. P. A., Italy.

Shen, X. H., Zhang, X. M., Yuan, S. G., Wang, L. W., Cao, J. B., Huang, J. P., Zhu, X. H., Piergiorgio, P., and Dai, J. P. (2018). The state-of-the-art of the China Seismo-Electromagnetic Satellite mission. *Sci. China Technol. Sci.*, *61*(5), 634–642. https://doi.org/10.1007/s11431-018-9242-0

Whaler, K. A., Hammer, M. D., Finlay, C. C., and Olsen, N. (2022). Core surface flow changes associated with the 2017 Pacific geomagnetic jerk. *Geophys. Res. Lett.*, *49*(15), e2022GL098616. https://doi.org/10.1029/2022GL098616

Winch, D. E., Ivers, D. J., Turner, J. P. R., and Stening, R. J. (2005). Geomagnetism and Schmidt quasi-normalization. *Geophys. J. Int.*, *160*(2), 487–504. https://doi.org/10.1111/j.1365-246X.2004.02472.x

Yan, Q., Ou, J. M., Suo, L., Jiang, Y., and Liu, P. F. (2023). Study on the estimation of Euler angles for Macau Science Satellite-1. *Earth Planet. Phys.*, *7*(1), 144–150. https://doi.org/10.26464/epp2023017

Yang, Y. Y., Hulot, G., Vigneron, P., Shen, X. H., Zhima, Z., Zhou, B., Magnes, W., Olsen, N., Tøffner-Clausen, L., … Zhu, X. H. (2021a). The CSES global geomagnetic field model (CGGM): An IGRF-type global geomagnetic field model based on data from the China Seismo-Electromagnetic Satellite. *Earth Planets Space*, *73*(1), 45. https://doi.org/10.1186/s40623-020-01316-w

Yang, Y. Y., Zhou, B., Hulot, G., Olsen, N., Wu, Y. Y., Xiong, C., Stolle, C., Zhima, Z., Huang, J. P., … Shen, X. H. (2021b). CSES high precision magnetometer data products and example study of an intense geomagnetic storm. *J. Geophys. Res.: Space Phys.*, *126*(4), e2020JA028026. https://doi.org/10.1029/2020ja028026

Yang, Y. Y., Wang, J., Zhima, Z., Shen, X. H., Zhou, B., Yuan, S. G., Miao, Y. Q., and Xu, Y. (2024). Advancements in low Earth orbit satellite magnetic field measurements and global geomagnetic field modeling. *Rev. Geophys. Planet. Phys. (in Chinese)*, *55*(6), 652–667. https://doi.org/10.19975/j.dqyxx.2023-054

Yi, S. Q., Xu, X. J., Zhou, Z. L., Chang, Q., Wang, X., Luo, L., He, P. S., and Li, H. (2023). Theoretical study of the ionospheric dynamo region inside the South Atlantic Anomaly. *Earth Planet. Phys.*, *7*(1), 84–92. https://doi.org/10.26464/epp2023015

Zhang, K. (2023). A novel geomagnetic satellite constellation: Science and applications. *Earth Planet. Phys.*, *7*(1), 4–21. https://doi.org/10.26464/epp2023019